

## A 256 x 256, 100-kfps, 61% Fill-Factor SPAD Image Sensor for Time-Resolved Microscopy Applications

### Citation for published version:

Gyongy, I, Calder, N, Davies, A, Dutton, NAW, Duncan, RR, Rickman, C, Dalgarno, PA & Henderson, RK 2018, 'A 256 x 256, 100-kfps, 61% Fill-Factor SPAD Image Sensor for Time-Resolved Microscopy Applications', *IEEE Transactions on Electron Devices*, vol. 65, no. 2, pp. 547-554.  
<https://doi.org/10.1109/TED.2017.2779790>

### Digital Object Identifier (DOI):

[10.1109/TED.2017.2779790](https://doi.org/10.1109/TED.2017.2779790)

### Link:

[Link to publication record in Heriot-Watt Research Portal](#)

### Document Version:

Peer reviewed version

### Published In:

IEEE Transactions on Electron Devices

### Publisher Rights Statement:

This work is licensed under a Creative Commons Attribution 3.0 License. For more information, see <http://creativecommons.org/licenses/by/3.0/>

### General rights

Copyright for the publications made accessible via Heriot-Watt Research Portal is retained by the author(s) and / or other copyright owners and it is a condition of accessing these publications that users recognise and abide by the legal requirements associated with these rights.

### Take down policy

Heriot-Watt University has made every reasonable effort to ensure that the content in Heriot-Watt Research Portal complies with UK legislation. If you believe that the public display of this file breaches copyright please contact [open.access@hw.ac.uk](mailto:open.access@hw.ac.uk) providing details, and we will remove access to the work immediately and investigate your claim.

# A $256 \times 256$ , 100-kfps, 61% Fill-Factor SPAD Image Sensor for Time-Resolved Microscopy Applications

Istvan Gyongy<sup>1</sup>, Neil Calder, *Member, IEEE*, Amy Davies, Neale A. W. Dutton, *Member, IEEE*, Rory R. Duncan, Colin Rickman, Paul Dalgarno, and Robert K. Henderson, *Senior Member, IEEE*

**Abstract**—A  $256 \times 256$  single-photon avalanche diode image sensor operating at 100 kfps with fill factor of 61% and pixel pitch of  $16 \mu\text{m}$  is reported. An all-nMOS 7T pixel allows gated operation down to 4 ns and  $\sim 600$ -ps fall time with on-chip delay generation. The sensor operates with 0.996 temporal aperture ratio in rolling shutter. Gating and cooling allow the suppression of dark noise, which, in combination with the high fill factor, enables competitive low-light performance with electron multiplying charge-coupled devices while offering time-resolved imaging modes.

**Index Terms**—CMOS single-photon avalanche diode (SPAD), quanta image sensor, single-photon counting (SPC), switched current source (SCS) counter.

## I. INTRODUCTION

SINGLE-PHOTON avalanche diode (SPAD) image sensors offer photon shot noise limited performance with picosecond timing resolution for applications in fluorescence lifetime imaging microscopy (FLIM), time-of-flight (ToF) 3-D imaging, and spectroscopy [1]. One of the key parameters of the devices is the external quantum efficiency (EQE), traditionally defined as the ratio of the photoelectrons produced by a pixel to the number of photons incident on the pixel area. For SPADs, EQE can be considered as the number of SPAD firings to incident photons, and has been historically limited by the low fill factor and large pixel pitches required by the complex digital pixel electronics necessary to

count and time the SPAD pulses. Analog circuit approaches or single-bit quanta pixels have considerably simplified the pixel electronics replacing counting or full-well capacity with oversampled readout and external frame summation [2], [3]. The resulting improvements in EQE have been considerable but are still an order of magnitude lower than the best electron multiplying charge-coupled device (EMCCD) or back-side illuminated (BSI) sCMOS sensors. Further improvements in sensitivity are therefore required to match EMCCD or sCMOS performance in low-light imaging applications, such as single molecule localization microscopy, and to attain faster FLIM and ToF acquisition than is possible with existing SPAD sensors.

One of the ways of increasing the EQE is to apply high excess bias voltage to the SPAD, resulting in improved SPAD photon detection probability (PDP). However, the gains that can be achieved (before the PDP saturates) may be limited, and the approach necessitates measures such as capacitive or cascode coupling [4], [5] are required to enable integration with front-end circuits, which can then impact the fill factor of the array. Ultimately, to achieve high EQE, the fill factor has to be optimized. Design approaches to facilitate this include stacking and BSI [6], and microlensing [3]. The potential downsides are a changed spectral response when moving to a stacked structure, and possible uneven coupling, and fabrication challenges, resulting from a microlens array. In the device presented in this paper, the fill factor is enhanced by the optimization of the detector and pixel circuit. The resulting sensor (Fig. 1) achieves a peak EQE of around 24% at 480 nm and 3-V excess bias, which is one of the highest reported values among SPAD image sensors. A consequence of having a large detector active area is increased dark count noise, compared to moving to a smaller pixel pitch and recovering fill factor using microlenses. However, in the SPAD structure adopted here, the dark count rate (DCR) can be substantially reduced by cooling, as widely used in scientific cameras.

The device, fabricated using STMicroelectronics' 130-nm imaging process technology [7], was first described in [8], and is presented here in expanded form with new microscopy results and additional characterization. A 7T all-nMOS pixel with  $16\text{-}\mu\text{m}$  pitch is designed, achieving 61% fill factor,

Manuscript received June 21, 2017; revised September 10, 2017 and November 20, 2017; accepted November 29, 2017. This work was supported by the European Research Council through the EU's Seventh Framework Program (FP/2007-2013)/ERC under Grant 339747. The review of this paper was arranged by Editor A. Lahav. (Corresponding author: Istvan Gyongy.)

I. Gyongy, N. Calder, and R. K. Henderson are with The University of Edinburgh, Edinburgh EH9 3JL, U.K. (e-mail: istvan.gyongy@ed.ac.uk; neil.calder@ed.ac.uk; robert.henderson@ed.ac.uk).

A. Davies, R. R. Duncan, C. Rickman, and P. Dalgarno are with Heriot-Watt University, Edinburgh EH14 5AS, U.K. (e-mail: amy.davies@hw.ac.uk; r.r.duncan@hw.ac.uk; c.rickman@hw.ac.uk; p.a.dalgarno@hw.ac.uk).

N. A. W. Dutton is with the Imaging Division, STMicroelectronics, Edinburgh EH3 5DA, U.K. (e-mail: neale.dutton@st.com).

Color versions of one or more of the figures in this paper are available online at <http://ieeexplore.ieee.org>.

Digital Object Identifier 10.1109/TED.2017.2779790

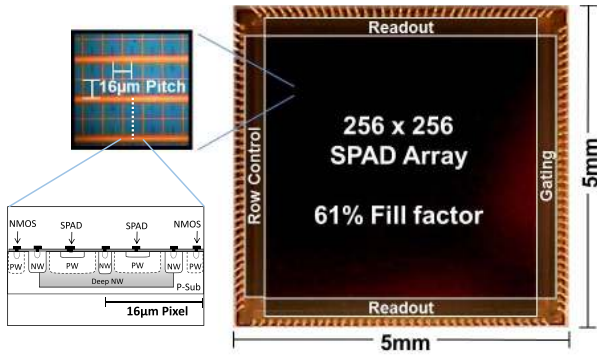


Fig. 1. Micrograph of image sensor and cross section of SPAD structure.

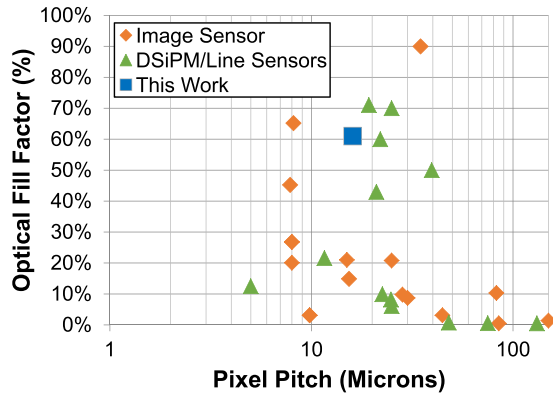


Fig. 2. Comparison with a representative set of existing SPAD sensors, indicating the fill factor achieved at different pixel sizes. (Native, non-microlensed, fill factors are plotted).

which compares well not only with state-of-the-art multipixel photon counters, but also densely packed nonimaging silicon photomultiplier (SiPM) arrays (see Fig. 2). Pixel bias voltage settings allow simultaneous optimization of readout settling time while achieving a 4-ns gate with a uniformly distributed  $\sim 600$ -ps fall time. The frame rate of 100 kfps ensures that there is practically no readout pile-up, and hence no loss of photons, in typical microscopy usage scenarios of around 10-k photons/s/pixel at output aggregate video rates of 10 frames/s.

## II. SENSOR ARCHITECTURE

The sensor is implemented in 130-nm 1P4M CMOS image sensor technology; a 90-nm process is used for back-end metallization. With the maximization of fill factor being a priority in the design of the chip, deep N-well sharing is used between pairs of SPAD rows (Fig. 1). Furthermore, the compact 7T all-nMOS pixel architecture depicted in Fig. 3 is implemented. This is a reduced version of the 9T pixel in [9], optimized here for binary operation. A  $\sim 10$ -fF memory capacitor  $C$ , formed using metal fringe capacitance to ground, is used to store the binary output of either 0 (no detected photon) or 1 (for at least one detected photon). The pixels are readout via dynamic comparators at the ends of the columns (situated in an alternating top/bottom pattern) with a 40-ns line time (Fig. 4). Readout noise is negligible due to the large voltage swing resulting from a photon detection. To reduce pixel supply droop at high photon detection rates, the supplies

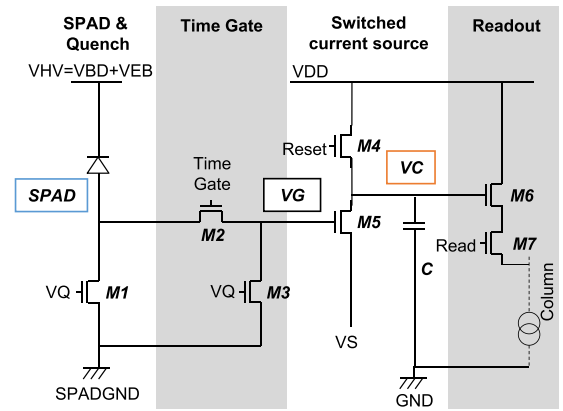


Fig. 3. Pixel architecture, highlighting the voltage nodes SPAD, VG, and VC.

VHV, SPADGND, and VDD are gridded with as much metal as possible without affecting the fill factor. A 64-bit-wide, 100-MHz digital output bus is used to read the bit-plane data off-chip at 6.4 Gb/s. Each output bus serves four pixel columns, transferred using 4-bit serializers. The range of pixel row readout may be reduced to a region of interest (ROI) to increase the frame rate. Exposures are captured using rolling or global electronic shutter. An on-chip programmable time-gate generator produces a global gate signal triggered by an external sync signal. The individual line reset and read signals are generated by a linear shift register. In the test results presented here, the necessary control and clocking signals (and chip configuration) for acquiring image frames were handled by a field-programmable gate array board (Opal Kelly XEM6310). The board is capable of continuous data streaming, at rates of  $> 100$  Mb/s, when the on-board SDRAM chip is used as an output buffer.

With the raw output consisting of binary frames, or bit planes, captured at a fast rate, the sensor can be considered as an example of a quanta image sensor [10] (in other words, an oversampled binary camera). Conventionally, “grayscale” frames can be produced by aggregating bit planes in time and/or space. This offers flexibility in (off-chip) image composition, and different methods of aggregation may be preferable depending on the application, including the following.

- 1) *Adaptive Summation* [11]: Rather than summing fixed groups of bit planes in time, a longer sum is used for static regions of a scene (to get high bit depth), and shorter sum is used for dynamic regions to prevent motion blur.
- 2) *Signal-Only Summation* [12]: A signal-only sum is carried out for blinking objects within a scene, so that background noise is minimized.
- 3) *Motion-Compensated Summation* [13]: Bit planes are transformed (e.g., shifted in space) prior to aggregation to compensate for motion artifacts.

Regardless the method of aggregation, there is no additional noise penalty, due to the absence of read noise on the individual bit planes. Furthermore, the shot noise on low photon count images may be compressed using postprocessing [14].

An important performance metric for low-light imagers is the temporal aperture ratio (TAR) [15], so the percentage of

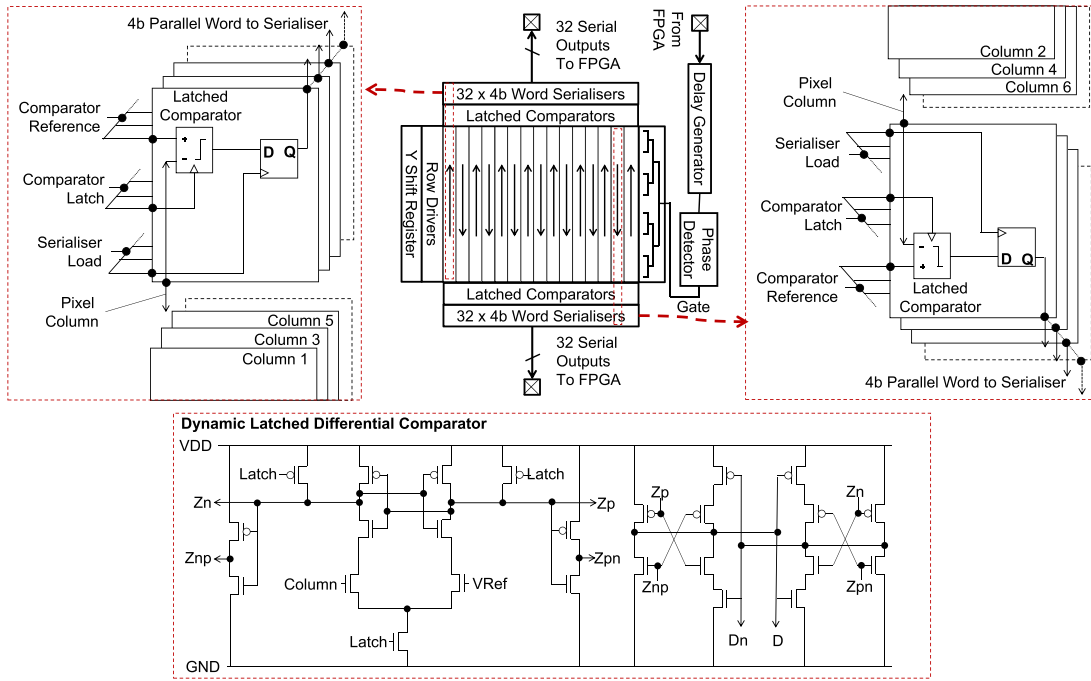


Fig. 4. Readout architecture and schematic of comparators.

the time that a sensor is able to collect/detect photons, when taking a sequence of images. Strictly speaking, in the case of a SPAD sensor, the TAR should encompass the SPAD dead time. However, in low-light applications such as life science fluorescence microscopy (where the photon detection rate is typically  $<0.1$  photons/pixel/bit plane), there is negligible readout pile-up (from binary counting), let alone dead-time pile-up (SPAD saturation). Thus, in rolling shutter mode (with back-to-back exposures at the native frame rate of 100 kfps), the TAR is only impacted by the line readout time of 40 ns, resulting in a high ratio of 0.996. This is useful in photon starved applications, where ideally a sensor should be constantly “aware” and collecting photons.

EMCCD and intensified charge-coupled device (ICCD) sensors typically have much lower TAR values (as low as 0.5 depending on the frame rate) due to significant readout dead time. While ICCD devices are capable of gating, they cannot operate with a rolling shutter, which in the case of SPADs enables an efficient gated operation in terms of minimizing the total acquisition time.

### III. PIXEL OPERATION AND GATING

The pixel circuit is shown in Fig. 3 and has four main parts:

- 1) a SPAD with passive quenching, which produces a voltage pulse whenever the SPAD triggers;
- 2) time-gating circuitry;
- 3) a switched current source (SCS), controlled by the time-gated SPAD pulse, which discharges capacitor  $C$ ;
- 4) a source follower to buffer the voltage  $VC$  of the capacitor onto the column line.

The quench voltage  $VQ$  and source voltage  $VS$  have significant bearing on the operation of the circuit, especially on the rise time of the time gate. As indicated in Fig. 5, SPAD pulses have a relatively long tail, so to achieve sharp time gating, one

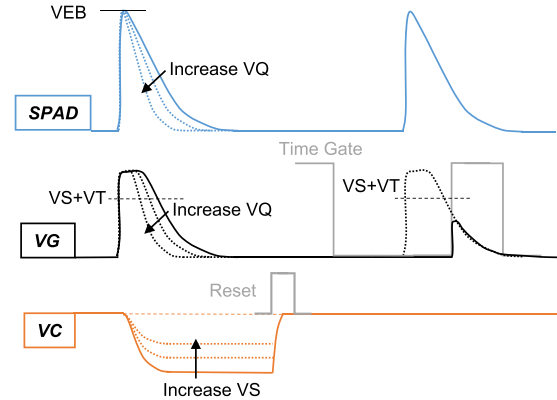


Fig. 5. Example voltage waveforms for pixel circuitry, indicating the effect of varying  $VQ$  and  $VS$ . As a result of the time gate shown, only the tail of the second SPAD pulse is seen at  $VG$ , and as it is lower than  $VS$  plus the transistor threshold voltage  $VT$ , the pulse is not registered.

must ensure that only SPAD events where the main pulse—rather than just the tail of the response—falls within the time gate enable signal are registered. Increasing  $VQ$  shortens the tail of the SPAD pulse, while increasing  $VS$  raises the voltage threshold required to activate the SCS. Both actions therefore result in the actuation of the current source becoming increasingly reliant on the peak of the SPAD pulse, leading to sharper gating. However, too high a  $VQ$  or  $VS$ , and the current source will not be switched ON for long enough (if at all), or draw away enough charge from  $VC$ , for all SPAD pulses to be registered. Loss of sensitivity therefore occurs, necessitating a careful balance to be struck in the choice of  $VQ$  and  $VS$ .

Figs. 6 and 7 show experimental data showing the effect of  $VS$  and  $VQ$ , respectively, on the effective time gate. The results were obtained by imaging the diffused light from a pulsed laser (Hamamatsu PLP-10 with 650-nm wavelength,



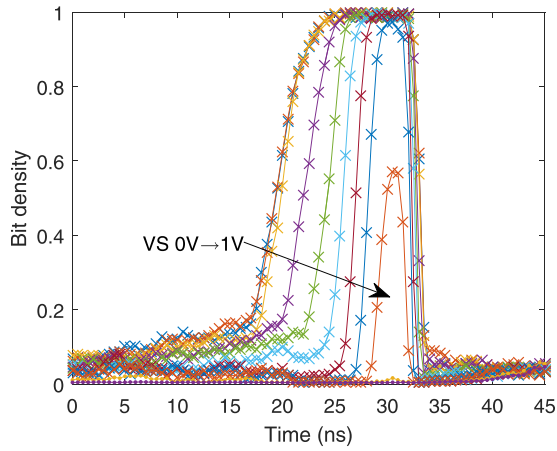


Fig. 6. Time gate profile for varying VS ( $V_Q = 1.3$  V and  $V_{HV} = 16$  V). Each data point corresponds to the mean pixel value, calculated for the whole array, based on 1000 bit-plane exposures. At high VS, the time gate edges are seen to become “eroded,” indicating a loss in sensitivity.

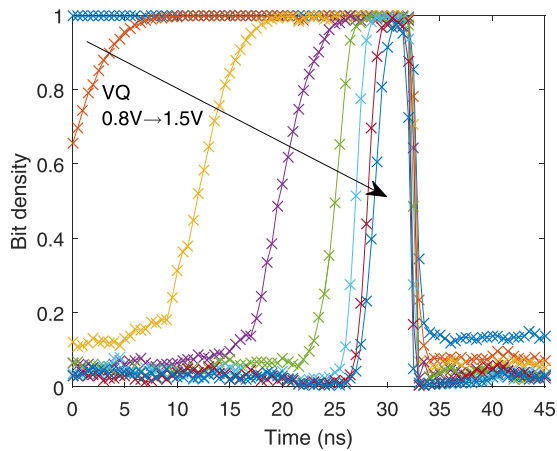


Fig. 7. Time-gate profile for varying VQ ( $V_S = 0.6$  V and  $V_{HV} = 16$  V). Data points refer to the mean pixel value over the whole array. The results indicate that a 4-ns time gate (full-width at half-maximum) with  $\sim 600$ -ps fall time is achievable.

<100-ps pulse duration laser head), whose sync signal, delayed in time by a delay generator (SRS DG645), was used to trigger the time gate of the sensor. For each voltage setting, the time delay was swept across a range of values to obtain the time gate profile. The results indicate an optimized time gate that is comparable to other SPAD image sensors [16], and is ideal for selectively time gating the common fluorophores used in microscopy, which typically have a fluorescent lifetime between 0.5 and 4 ns [17]. The temporal mismatches in the rising and falling edges of the time gate across are characterized in Figs. 8 and 9; offsets of 3 ns and  $\approx 500$  ps are seen, respectively. In the case of the leading edge, the profile of the mismatch may be explained by self-heating on the sensor affecting the SPAD dead time, whereas for the falling edge, the transit time of the gate signal (introduced from the left side of the array) is observed.

Aside from its role in optimizing the time gate, another important function of VS is reducing the voltage swing on VC and thereby accelerating settling on the column line, thus increasing the frame rate. Furthermore, an elevated

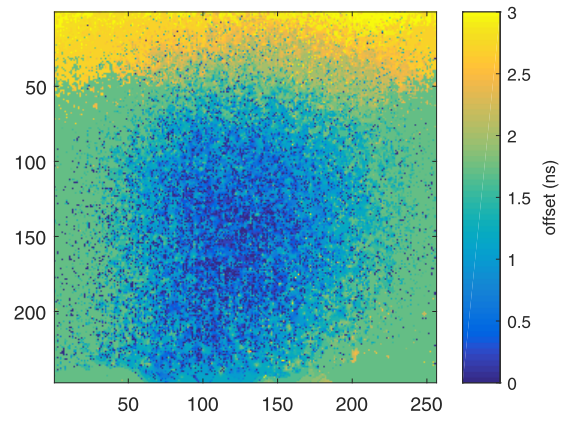


Fig. 8. Mismatch in rising edge of time gate, in terms of time to rise above half maximum ( $V_S = 0.6$  V,  $V_Q = 1.3$  V, and  $V_{HV} = 16$  V).

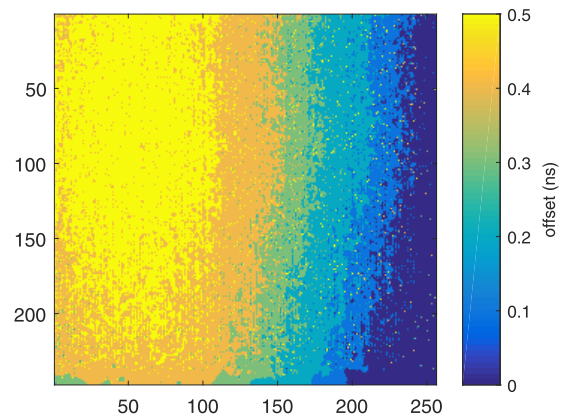


Fig. 9. Mismatch in falling edge of time gate, in terms of time to fall below half maximum ( $V_S = 0.6$  V,  $V_Q = 1.3$  V, and  $V_{HV} = 16$  V).

VS practically eliminates pixel leakage, as the MOS M5 is then in the cutoff region, minimizing electron transfer between drain and source.

#### IV. NOISE AND NONUNIFORMITIES

The main source of noise affecting exposures is the DCR, or spurious firing rate, of the pixels, due to thermal generation effects. The level of DCR is dependent on both the excess bias applied to the SPADs (the bias above reverse breakdown voltage) and temperature. Fig. 10 shows the median DCR for different excess bias values, as the chip cooled from room temperature down to  $-5$  °C using a Peltier device. The DCR is seen to reduce by an order of magnitude as a result of cooling. This is consistent with [18] involving similar SPAD structures, which suggested a halving of DCR for every 8 °C temperature drop. By operating the camera in gated mode, the effective DCR is further reduced, in proportion to the duty cycle of the time gate. Assuming a 10-ns time gate, at 10-MHz repetition rate and 1.5-V excess bias, we get a median dark count of around 60 Hz at  $-5$  °C, enabling an intrasene dynamic range [10], when aggregating 10- $\mu$ s bit-plane exposures, of  $\approx 20$  dB  $\times \log(1/(6 \times 10^{-4})) = 64.4$  dB.

Optical crosstalk is another significant noise source in closely packed SPAD arrays. It is caused by hot carriers generated in avalanche event recombining and emitting photons which are then, in turn, absorbed by neighboring SPADs,

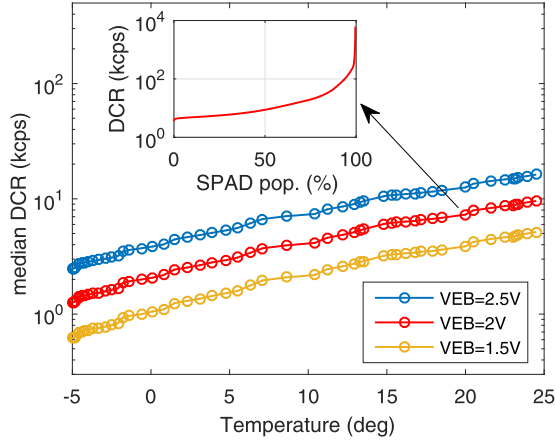


Fig. 10. Median DCR plotted as a function of temperature at different excess bias settings. Inset shows the cumulative distribution of the dark count at 1.5-V excess bias and 20°.

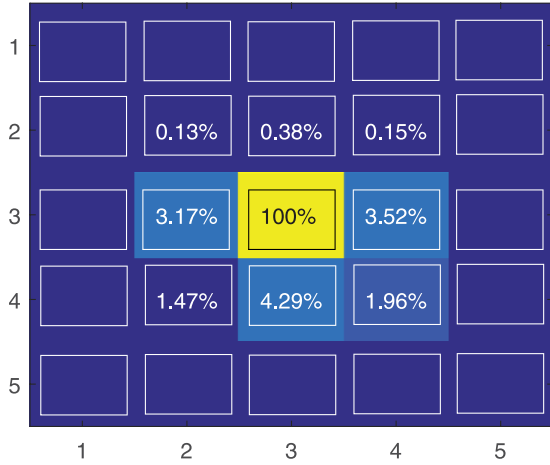


Fig. 11. Approximate crosstalk probability map, as obtained at room temperature and 1.5-V excess bias, based on 116 hot pixels (with DCRs between 1 and 10 MHz).

triggering additional avalanches. In the present SPAD sensor, direct measurement of crosstalk is not possible, as the output of the detectors cannot be directly probed (nor can they be individually enabled). An approximate, indirect approach was therefore adopted. A DCR map was created by summing a sequence of  $2 \times 10^6$  bit planes obtained in dark conditions (the dark counts being linearized to account for logarithmic compression [19]). Hot pixels were then identified, and the average rise in counts in adjacent pixels was determined. The resulting estimates for the crosstalk probability, measured at an excess bias of 1.5 V, are given in Fig. 11. They indicate a maximum probability of around 4%, which increases to approximately 10% at 3-V excess bias. This is in line with the mean crosstalk probability of 4% between nearest neighbors, as measured in [20] for a similar SPAD structure (although with a slightly lower fill factor of 48.5%). It is interesting to note that crosstalk is mostly confined to within the “paired” rows of the array, so it tends to occur through the shared N-well, and not the nMOS electronics. A potential technique for addressing crosstalk is deep trench isolation [21], as commonly used in SiPMs.

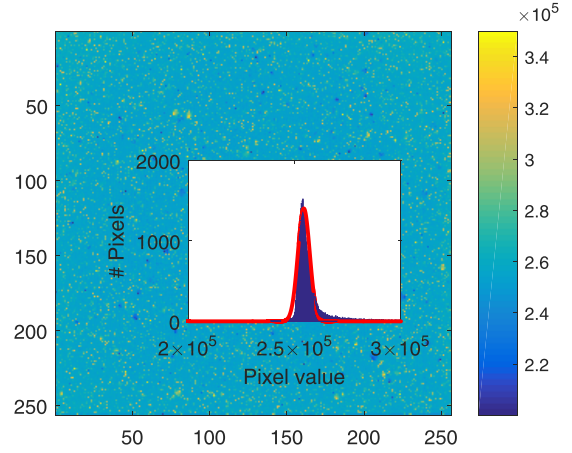


Fig. 12. Sum of  $2 \times 10^6$ , 2- $\mu$ s bit-plane exposures under uniform illumination at a wavelength of 550 nm, at room temperature and excess bias of 1.5 V. A DCR map has been subtracted from the image frame, and hot pixels ( $\approx 1\%$  of pixels) are interpolated over. Inset shows the maximum likelihood Gaussian fit to the histogram of pixel values.

Another source of correlated noise is SPAD afterpulsing, due to carriers that get trapped during an avalanche process, and are then released, triggering another avalanche. In a binary SPAD sensor operated in nongated configuration, afterpulses will tend to occur within the same exposure as the original pulse (due to an exposure time  $\gg$  SPAD dead time), in which case they are not counted. The impact is therefore likely to be small. In time-gated operation, afterpulsing has the effect of introducing additional uncertainty (reduced sharpness) in the leading edge of the time gate.

The uniformity in the response of the array was measured under uniform illumination resulting in a median photon detection rate of around 50 kHz/pixel (Fig. 12). The standard deviation in the response, after DCR correction, is found to be around 1.1% at wavelengths of 450 and 550 nm. It is likely that most of this variability arises from differences in the SPAD breakdown voltages between individual detectors.

Due to the irregular spacing of the detectors (the centers being 16  $\mu$ m apart in the  $x$ -direction; the spacing alternating between 13.41 and 18.59  $\mu$ m in the  $y$ -direction), another nonuniformity to account for is in the modulation transfer function (MTF) of the sensor (quantifying the magnitude response to different spatial frequencies). The detector MTF was computed numerically, approximating the active areas as squares with uniform photon detection efficiency. According to this calculation, the MTF along  $y$  is 10% higher than that in  $x$  at the Nyquist sampling frequency (0.79 versus 0.72).

## V. MICROSCOPY RESULTS

### A. Fluorescence Lifetime Imaging

The sensor was used to image a *Convallaria* rhizome test slide (AS321, Johannes Lieder, Germany) on an Olympus IX71 microscope, with excitation being provided by a pulsed laser (Picoquant LDH with 405-nm wavelength laser head) set to a 5-MHz repetition rate. The sync signal from the laser was supplied directly to the camera to trigger a 15-ns time gate. Reference (nontime gated) images were captured the

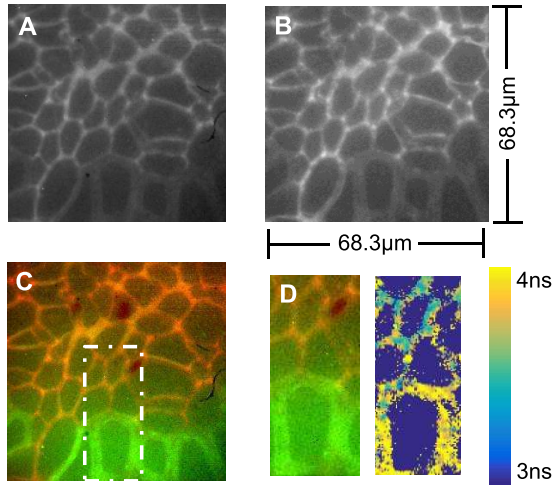


**Fig. 13.** Convallaria slide, as observed through a  $\times 60$  objective, and imaged using (A) SPAD sensor (15-ns time gate, VHV = 16.5 V) in the red channel, (B) sCMOS in the red channel, (C) SPAD (overlay of red and green channels), and (D) fluorescence lifetime map estimated from ten SPAD image frames, each obtained with a different time delay with respect to the laser excitation. SPAD images are composed by summing 25 000, 10- $\mu$ s bit-plane exposures (for a total exposure time of 250 ms). Hot pixel and background compensation have been applied.

same field of view, by an sCMOS camera (Hamamatsu ORCA-Flash4.0).

**Fig. 13(A)** shows the SPAD image that is obtained from the red channel when the camera time gate encompasses the fluorescent response of the sample. The image is comparable to the corresponding sCMOS output [**Fig. 13(B)**], though the latter does shown more detail, due to the smaller pixel size (6.5- $\mu$ m pixel pitch) of the sCMOS device. Furthermore, the sCMOS image has less photon shot noise; the extracted total photon count being around 10 times higher than that from the SPAD PDP at red wavelengths, and the sCMOS capturing photos outside the SPAD time gate. Capturing SPAD images in both the red and green channels and overlaying the two images leads to **Fig. 13(C)**, showing distinct green and red (or orange) regions in the sample.

The advantage of the SPAD device is the ability to characterize the fluorescent response of the specimen, by sliding the time gate with respect to the laser pulse. In this case, a set of ten image frames were obtained, the delay of the time gate being increased in steps of 1.5 ns so as to capture the decay in fluorescent response across the field of view. Pixel values were binned in groups of  $10 \times 10$ , and an exponential fit, to describe the resulting variation in time (i.e., estimate the fluorescence lifetime). **Fig. 13(D)** compares the resulting lifetime map, over a subregion of the field of view, to the corresponding two-color intensity image. An apparent difference in lifetimes can be seen between the mostly green and red dominated areas of the sample. To assess the precision of lifetime estimates, a similar imaging experiment was carried out on a cuvette of fluorescein, with a time-correlated single-photon counting sensor [22] providing a reference lifetime value of 3.90 ns ( $R^2 = 0.96$ ). In comparison, the present sensor measured a mean lifetime value of 3.92 ns, with a standard deviation of 2% across the array (**Fig. 14**).

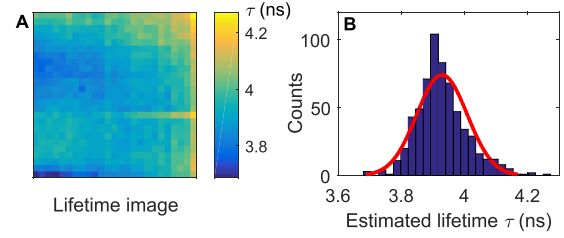


**Fig. 14.** Measuring the lifetime of a uniform fluorescein sample. (A) Lifetime map obtained by moving a 15-ns time gate in 1-ns steps (exploiting the sharper, falling edge), and composing ten image frames, from 10 000, 10- $\mu$ s bit-plane exposures each, using  $10 \times 10$  pixel binning. (B) Histogram of lifetime estimates across the array. The pooled, temporal standard deviation of the lifetime values for repeated measurements was found to be approximately 1%.

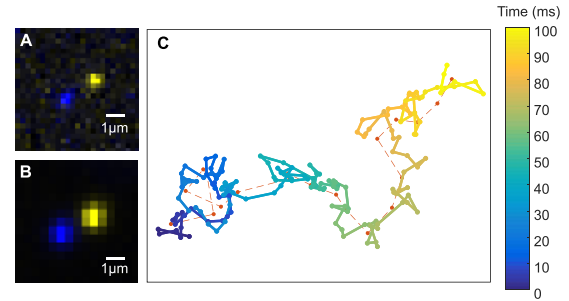


**Fig. 15.** Tracking a fluorescent bead over a 100-ms time interval. (A) First (blue) and last (yellow) images from SPAD camera. (Each image is composed of 200, 25- $\mu$ s bit planes, giving a 0.5-ms exposure.) (B) First (blue) and last (yellow) images from sCMOS camera (5-ms exposure). (C) Bead trajectories obtained with SPAD (colored line) and sCMOS (red dashed line), the small dots indicating the localized bead position on different image frames.

### B. Bead Tracking

In this test, the SPAD and sCMOS cameras were used to image a freely diffusing sample of 0.2- $\mu$ m diameter, red fluorescent beads (FluoSpheres Carboxylate-Modified Microspheres). The beads were suspended in water, within a microchannel at least 100  $\mu$ m high and several millimeters in breadth and width. Images were captured at room temperature, with the SPAD and sCMOS coupled to the microscope via a 50:50 beam splitter to enable simultaneous imaging of the same field of view. With the aim being to track the position of beads with high temporal resolution, the frame rate of the sCMOS device was increased to 200 frames/s using pixel binning and ROI cropping. With the SPAD camera, the frame rate (and exposure time) is set in postprocessing, according to the number of bit planes that is summed per image frame. It is therefore possible to obtain a higher frame rate than with the sCMOS device by reducing the level of aggregation. This is illustrated in **Fig. 15**, which shows the results of tracking a given fluorescent bead based on 2-kfps SPAD versus 200 frames/s sCMOS image frames. The results relate to a 100-ms time period, with **Fig. 15(A)** and **(B)** showing (overlaid) images of the bead at the start (blue) and end (yellow) of this period, as captured with the SPAD and sCMOS, respectively. (Note that the field of view has been cropped for clarity.) **Fig. 15(C)** shows the trajectories obtained with the two devices (using the TrackMate ImageJ



TABLE I  
 COMPARISON OF HIGH QUANTUM EFFICIENCY SPAD IMAGE SENSORS

	[5]	[27]	[6]	[28]	[29]	[30]	[17]	This work
Technology	FSI 0.13μm	FSI 40nm	3D-BSI 40/65nm	FSI 0.13μm CIS	FSI 0.35μm HV	3D-BSI 0.13μm/ custom	FSI 0.35μm HV	FSI 0.13μm CIS
Array size	512×512	96×40	128×120	320×240	160×120	256×256	512×128	256×256
Pixel pitch	16.38μm	8.25μm	7.83μm	8μm	15μm	25μm	24μm	16μm
Microlens	No	No	No	Yes	No	No	Yes	No
Fill factor FF (collimated light)	13%	66%	45%	50%	21%	>90%	>50%	61%
Max. PDP	40% at 550nm (VEB=6.5V)	-	27.5% at 640nm (VEB=3V)	39.5% at 480nm (VEB=3V)	-	-	33.3% at 450nm (VEB=4.5V)	39.5% at 480nm (VEB=3V)
Maximum EQE=PDP×FF	5%	-	12%	20%	-	-	20%	24%
Median DCR (room temp.)	0.3cps/μm <sup>2</sup> (VEB=3.3V)	1.5cps/μm <sup>2</sup> (VEB=1V)	7.2cps/μm <sup>2</sup> (VEB=1V)	2.7 cps/μm <sup>2</sup> (VEB=1.5V)	11.3 cps/μm <sup>2</sup> (VEB=3V)	-	6.9 cps/μm <sup>2</sup> (VEB=3.5V)	40 cps/μm <sup>2</sup> (VEB=1.5V)

plugin [23]). The SPAD camera (colored line) is seen to capture the motion of the bead in considerably more detail than the sCMOS (red dashed line). This is a consequence of the mean free path of the Brownian motion of the particle scaling with the square root of the time interval between image frames. The 2-D mean free path is calculated from the SPAD frames as 60 nm, which is similar to the nominal value of 69 nm, as determined from theory [24]. The ability to track particles with high temporal resolution is important in a number of applications in microscopy, for example for studying the motion of molecules in the context of intercellular communication [25].

## VI. SNR COMPARISON

The signal-to-noise ratio (SNR) performance of the camera, in optimal conditions, was compared to the noise models for other camera technologies. With the dark count, which increases with exposure time, being the dominant source of noise, collecting photons in “short bursts” is preferable from an SNR perspective. Hence, the measurements were carried out in gated operation, with a reasonably high number of incident photons per time gate ( $\sim 0.25$  photons per 15-ns time gate). The dark count was further reduced by cooling the sensor to  $-5^\circ$ , making the dark count effectively negligible in comparison to true photon counts. A 450-nm continuous wave light source was used, generated by filtering a white LED (Thorlabs MCWHL5) with a 10-nm-wide bandpass filter (FB450-10). The incident light intensity on the sensor was measured using a calibrated power meter (Thorlabs PM200 with S120C sensor), and converted to photon flux based on the wavelength of the light.

Fig. 16 shows the SNR versus the mean number of incident photons (also known as the photon transfer curve). The data points, referring to a single pixel with median DCR, are based on a sequence of one million bit-plane exposures (each with a single, 15-ns time gate), acquired both with and without illumination. The SNR values are calculated from the output counts obtained by summing bit planes in groups of varying sizes. For each grouping (consisting of  $N$  groups of  $M$  bit

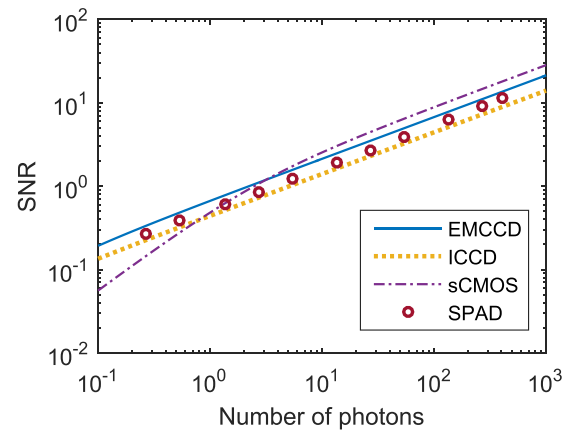


Fig. 16. Comparison of the measured photon transfer curve for the SPAD camera (at 3-V excess bias) with those of EMCCD, ICCD, and sCMOS (based on noise models). The assumed camera parameters (EQE, rms readout noise, gain, excess noise factor, and DCR) are as follows: EMCCD = (90%,  $20e^-$ , 200, 1.41, 0.001 Hz), ICCD = (50%,  $4.8e^-$ , 200, 1.6, 0.1 Hz), and sCMOS = (80%,  $1.4e^-$ , 1, 1, 0.05 Hz).

planes, where  $N \times M = 10^6$ ), the SNR is then given by

$$\text{SNR} = \frac{\text{mean}(\text{count}_{\text{light ON}}) - \text{mean}(\text{count}_{\text{light OFF}})}{\sqrt{\text{var}(\text{count}_{\text{light ON}})}}$$

with the corresponding number of incident photons being determined from the photon flux measurement.

Fig. 16 shows the comparison of the measured data points from the SPAD sensor with the photon transfer curves of EMCCD, ICCD, and sCMOS cameras, based on standard noise models used in [26]. Comparable SNR performance is observed, with the SPAD results lagging behind the EMCCD model only by around a factor of 1.4, but surpassing the ICCD, as well as the sCMOS for low numbers of incident photons.

It is noted that the implied difference in performance between the EMCCD and SPAD is in line with expectations given the specifications of the devices. The EQE of the EMCCD may be almost four times higher than that of the SPAD, but at typical EM gain settings (100–1000), the EMCCD is subject to an excess noise factor that effectively



halves the EQE. (More precisely, the shot noise variance is amplified by a factor of 2.) This leads to a factor of 2 difference in sensitivity between the EMCCD and SPAD, which translates to a  $\times\sqrt{2}$  difference in SNR (assuming negligible dark count and read noise in both devices). The fact that the SPAD data points in Fig. 16 lie in a straight line confirms that the sensor is shot noise limited, and read noise is negligible.

## VII. CONCLUSION

A SPAD image sensor designed for microscopy has been presented. By using compact pixels with binary output, the sensor achieves a fill factor and EQE that is among the highest in its class (Table I). The drawback of the large detector active area is increased crosstalk and dark noise, though the latter can be mitigated by cooling.

The sensor has the added functionality of time-resolved imaging, based around an on-chip programmable time gate. Potential applications therefore include FLIM as well as intensity imaging where a strong background fluorescence is to be suppressed through gating. The sensor also enables high-speed particle tracking. Outside microscopy, applications in ToF and quantum imaging are envisaged.

## ACKNOWLEDGMENT

The authors would like to thank STMicroelectronics who fabricated the chip. They would also like to thank Heriot-Watt University, Edinburgh, U.K., for the use of the ESRIC facilities.

## REFERENCES

- [1] E. Charbon, "Single-photon imaging in complementary metal oxide semiconductor processes," *Philos. Trans. Roy. Soc. London A, Math. Phys. Sci.*, vol. 372, p. 20130100, Feb. 2014, doi: [10.1098/rsta.2013.0100](#).
- [2] N. A. W. Dutton, I. Gyongy, L. Parmesan, and R. K. Henderson, "Single photon counting performance and noise analysis of CMOS SPAD-based image sensors," *Sensors*, vol. 16, no. 7, p. 1122, Jul. 2016, doi: [10.3390/s16071122](#).
- [3] I. M. Antolovic, S. Burri, R. A. Hoebe, Y. Maruyama, C. Bruschini, and E. Charbon, "Photon-counting arrays for time-resolved imaging," *Sensors*, vol. 16, no. 7, p. 1005, Jun. 2016, doi: [10.3390/s16071005](#).
- [4] E. A. G. Webster, L. A. Grant, and R. K. Henderson, "A high-performance single-photon avalanche diode in 130-nm CMOS imaging technology," *IEEE Electron Device Lett.*, vol. 33, no. 11, pp. 1589–1591, Nov. 2012, doi: [10.1109/led.2012.2214760](#).
- [5] A. C. Ulku, C. Bruschini, X. Michalet, S. Weiss, and E. Charbon, "A 512×512 SPAD image sensor with built-in gating for Phasor based real-time siFLIM," in *Proc. IISW*, 2017, pp. 234–237.
- [6] T. Al Abbas, N. A. W. Dutton, O. Almer, S. Pellegrini, Y. Henrion, and R. K. Henderson, "Backside illuminated SPAD image sensor with 7.83  $\mu\text{m}$  pitch in 3D-Stacked CMOS technology," in *IEDM Tech. Dig.*, Dec. 2016, pp. 8.1.1–8.1.4, doi: [10.1109/iedm.2016.7838372](#).
- [7] S. Pellegrini and B. Rae, "Fully industrialised single photon avalanche diodes," *Proc. SPIE*, vol. 10212, p. 102120D, May 2017, doi: [10.1117/12.2264364](#).
- [8] I. Gyongy *et al.*, "256×256, 100 kfps, 61% Fill-factor time-resolved SPAD image sensor for microscopy applications," in *IEDM Tech. Dig.*, Dec. 2016, pp. 8.2.1–8.2.4, doi: [10.1109/iedm.2016.7838373](#).
- [9] N. A. W. Dutton, L. Parmesan, A. J. Holmes, L. A. Grant, and R. K. Henderson, "320×240 oversampled digital single photon counting image sensor," in *VLSI Symp. Dig. Tech. Papers*, Jun. 2015, pp. 1–2, doi: [10.1109/vlsic.2014.6858428](#).
- [10] E. R. Fossum, "Modeling the performance of single-bit and multi-bit quanta image sensors," *IEEE J. Electron Device Soc.*, vol. 1, no. 9, pp. 166–174, Sep. 2013, doi: [10.1109/JEDS.2013.2284054](#).
- [11] I. Gyongy *et al.*, "Bit-plane processing techniques for low-light, high speed imaging with a SPAD-based QIS," in *Proc. IISW*, 2015, pp. 8–11.
- [12] I. Gyongy *et al.*, "Smart-aggregation imaging for single molecule localisation with SPAD cameras," *Sci. Rep.*, vol. 6, Nov. 2016, Art. no. 37349, doi: [10.1038/srep37349](#).
- [13] I. Gyongy, T. A. Abbas, N. A. W. Dutton, and R. K. Henderson, "Object tracking and reconstruction with a quanta image sensor," in *Proc. IISW*, 2017, pp. 242–245.
- [14] S. H. Chan, O. A. Elgandy, and X. Wang, "Images from bits: Non-iterative image reconstruction for quanta image sensors," *Sensors*, vol. 16, no. 11, p. 1961, Nov. 2016, doi: [10.3390/s16111961](#).
- [15] N. Teranishi, "Required conditions for photon-counting image sensors," *IEEE Trans. Electron Devices*, vol. 59, no. 8, pp. 2199–2205, Aug. 2012, doi: [10.1109/ted.2012.2200487](#).
- [16] M. Perenzoni, L. Pancheri, and D. Stoppa, "Compact SPAD-based pixel architectures for time-resolved image sensors," *Sensors*, vol. 16, no. 5, p. 745, May 2016, doi: [10.3390/s16050745](#).
- [17] M. Y. Berezin and S. Achilefu, "Fluorescence lifetime measurements and biological imaging," *Chem. Rev.*, vol. 110, pp. 2641–2684, May 2010, doi: [10.1021/cr900343z](#).
- [18] J. A. Richardson, "Time resolved single photon imaging in nanometer scale CMOS technology," Ph.D. dissertation, Univ. Edinburgh, Scotland, U.K., 2010.
- [19] I. M. Antolovic, S. Burri, C. Bruschini, R. Hoebe, and E. Charbon, "Nonuniformity analysis of a 65-kpixel CMOS SPAD imager," *IEEE Trans. Electron Devices*, vol. 63, no. 1, pp. 57–64, Jan. 2016, doi: [10.1109/ted.2015.2458295](#).
- [20] H. Xu, L. Pancheri, L. H. C. Braga, G.-F. D. Betta, and D. Stoppa, "Cross-talk characterization of dense single-photon avalanche diode arrays in CMOS 150-nm technology," *Opt. Eng.*, vol. 55, no. 6, p. 067102, Jun. 2016, doi: [10.1117/1.oe.55.6.067102](#).
- [21] N. D'Ascenzo, V. Saveliev, and Q. Xie, "Design and test of SiPM structures in CMOS technology," in *Proc. 4th Int. Conf. Photon., Opt. Laser Technol. (PHOTOPTICS)*, 2016, pp. 1–8, doi: [10.5220/0005746702130220](#).
- [22] A. T. Erdogan *et al.*, "A 16.5 Giga events/s 1024×8 SPAD line sensor with per-pixel zoomable 50 ps-6.4 ns/bin histogramming TDC," in *Proc. VLSI Symp.*, 2017, pp. C292–C293, doi: [10.23919/vlsic.2017.8008513](#).
- [23] J.-Y. Tinevez *et al.*, "TrackMate: An open and extensible platform for single-particle tracking," *Methods*, vol. 115, pp. 80–90, Feb. 2017, doi: [10.1016/j.ymeth.2016.09.016](#).
- [24] M. A. Catipovic, P. M. Tyler, J. G. Trapani, and A. R. Carter, "Improving the quantification of Brownian motion," *Amer. J. Phys.*, vol. 81, pp. 485–491, Jul. 2013, doi: [10.1119/1.4803529](#).
- [25] L. Yang *et al.*, "Secretory vesicles are preferentially targeted to areas of low molecular SNARE density," *PLoS ONE*, vol. 7, p. e49514, Nov. 2012, doi: [10.1371/journal.pone.0049514](#).
- [26] T. Resetar *et al.*, "Development of gated pinned avalanche photodiode pixels for high-speed low-light imaging," *Sensors*, vol. 16, no. 8, p. 1294, Aug. 2016, doi: [10.3390/s16081294](#).
- [27] T. Al Abbas *et al.*, "8.25  $\mu\text{m}$  pitch 66% fill factor global shared well SPAD image sensor in 40 nm CMOS FSI technology," in *Proc. IISW*, 2017, pp. 238–241.
- [28] I. Gyongy *et al.*, "Enhanced collection efficiency of SPAD imagers through the use of cylindrical microlenses," to be published.
- [29] M. Perenzoni, N. Massari, D. Perenzoni, L. Gasparini, and D. Stoppa, "A 160×120 pixel analog-counting single-photon imager with time-gating and self-referenced column-parallel A/D conversion for fluorescence lifetime imaging," *IEEE J. Solid-State Circuits*, vol. 51, no. 1, pp. 155–167, Jan. 2016, doi: [10.1109/jssc.2015.2482497](#).
- [30] B. Aull, "Geiger-mode avalanche photodiode arrays integrated to all-digital CMOS circuits," *Sensors*, vol. 16, no. 4, p. 495, Apr. 2016, doi: [10.3390/s16040495](#).

Authors' photographs and biographies not available at the time of publication.